iScience

CellPress
OPEN ACCESS

Article

Impaired phase separation and nucleolar functions in hiPSC models of *SNORD118*-related ribosomopathies

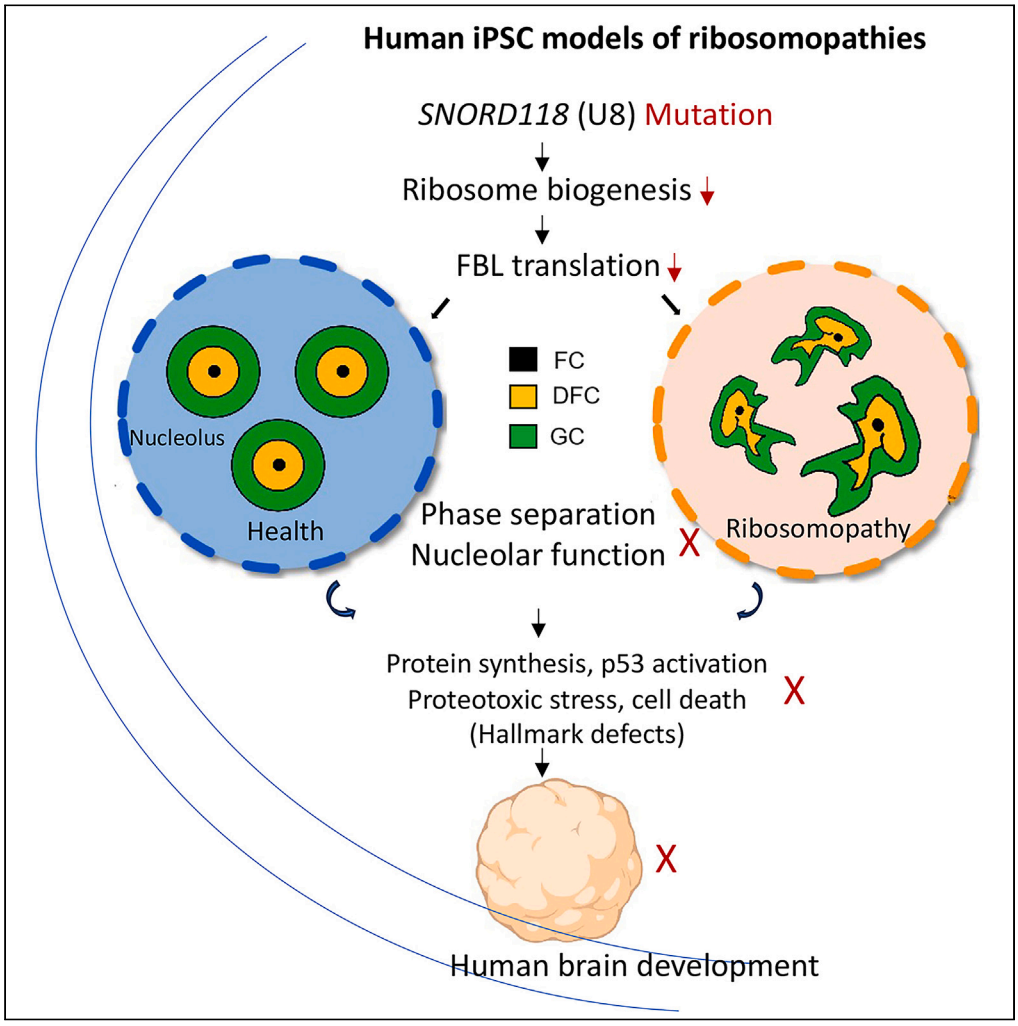

Wei Zhang, Minjie Zhang, Li Ma, ..., Ziying Lin, Zhipeng Lu, Jian-Fu Chen

jianfu@usc.edu

Highlights

SNORD118 mutant hiPSC-derived cells and organoids recapitulate the ribosomopathy defects

Mutations impair ribosome biogenesis and translation of phase separation effector FBL

Phase separation and nucleolar organization are defective in *SNORD118* mutant cells

Impaired phase separation causes ribosomopathy and growth defects in hiPSC models

Zhang et al., iScience *27*, 110430
August 16, 2024 Published by Elsevier Inc.
https://doi.org/10.1016/j.isci.2024.110430

iScience

CellPress
OPEN ACCESS

Article

Impaired phase separation and nucleolar functions in hiPSC models of *SNORD118*-related ribosomopathies

Wei Zhang,[1] Minjie Zhang,[2] Li Ma,[1] Supawadee Jariyasakulroj,[1] Qing Chang,[1] Ziying Lin,[1] Zhipeng Lu,[2] and Jian-Fu Chen[1,3,*]

SUMMARY

Ribosomopathies arise from the disruptions in ribosome biogenesis within the nucleolus, which is organized via liquid-liquid phase separation (LLPS). The roles of LLPS in ribosomopathies remain poorly understood. Here, we generated human induced pluripotent stem cell (hiPSC) models of ribosomopathy caused by mutations in small nucleolar RNA (snoRNA) gene SNORD118. Mutant hiPSC-derived neural progenitor cells (NPCs) or neural crest cells (NCCs) exhibited ribosomopathy hallmark cellular defects resulting in reduced organoid growth, recapitulating developmental delay in patients. SNORD118 mutations in NPCs disrupted nucleolar morphology and LLPS properties coupled with impaired ribosome biogenesis and a translational downregulation of fibrillarin (FBL), the key LLPS effector acting via the intrinsically disordered region (IDR) motif. IDR-depleted FBL failed to rescue NPC defects, whereas a chimeric FBL with swapped IDR motif from an unrelated protein mitigated ribosomopathy and organoid growth defects. Thus, SNORD118 human iPSC models revealed aberrant phase separation and nucleolar functions as potential pathogenic mechanisms in ribosomopathies.

INTRODUCTION

Ribosomopathies are a heterogeneous group of human disorders caused by mutations in ribosome biogenesis factors.[1,2] An increasing number of studies have revealed the consensus about the ribosomopathy hallmark cellular defects, such as protein synthesis loss, p53 activation, and proteotoxicity.[1,3,4] The exact mechanisms that reconcile the protein loss with proteotoxic stress are under active investigation. The disease phenotypes are divergent among different ribosomopathies but tend to affect specific cells/tissues such as blood and skeletal tissues,[1,5] on which most past research has been focused. Ribosome biogenesis is a housekeeping process required for all cells and tissues in the body, and how the disruption of a ubiquitous process leads to tissue-specific defects remains an outstanding question.[1,2,5] In this regard, the brain is an organ with relatively fewer investigations compared to other organs in terms of ribosome biogenesis regulation and function. In addition, human and mouse brain structure and function exhibit differences to a certain degree. The human brain undergoes an evolutionary expansion in development due to the primate-enriched outer subventricular zone (oSVZ).[6] Human-induced pluripotent stem cells (hiPSCs) and hiPSC-derived brain organoids provide a platform for experimentally addressing early human neurodevelopmental processes associated with neuropsychiatric disorders in a relevant genetic and cellular context.[6–8] However, brain organoids have not been extensively used to study ribosomopathies. Overall, ribosome biogenesis in human brain ribosomopathies remains poorly understood.

Ribosome biogenesis occurs in the nucleolus, which is a non-membrane or membrane-less organelle. The nucleolus has three layers: the inner fibrillar center (FC), where rDNA is transcribed into rRNA precursor; the dense fibrillar component (DFC), where rRNA processes and modification occur; and the granular component (GC), where the ribosomal subunits assemble. Without membrane-mediated physical separation, these three layers in the nucleolus are spatially organized through liquid-liquid phase separation (LLPS) of their molecular components.[9,10] The intrinsically disordered regions (IDRs) within nucleolar molecular components drive the condensation of these components into a separate phase underlying the assembly of the nucleolus.[9,10] The condense is characterized by unique biophysical properties including the surface tension, which is critical for the organized demixing of nucleolar sub-compartments. LLPS provides a conceptual framework for the organization of nucleolus. However, little is known about how LLPS impairment is linked with ribosomopathy hallmark cellular defects.

Human genetic studies identified the first brain ribosomopathy disorder with exclusive pathologies in the CNS due to the mutations in *SNORD118*.[11,12] *SNORD118* brain ribosomopathy patients exhibit a wide range of phenotypes, such as growth delay, mental retardation, cerebral white matter defects, as well as cognitive and motor dysfunctions.[11,12] *SNORD118* encodes U8, a noncoding RNA belonging to the

[1]Center for Craniofacial Molecular Biology, University of Southern California, Los Angeles, CA 90033, USA
[2]Department of Pharmacology and Pharmaceutical Sciences, University of Southern California, Los Angeles, CA 90089, USA
[3]Lead contact
*Correspondence: jianfu@usc.edu
https://doi.org/10.1016/j.isci.2024.110430

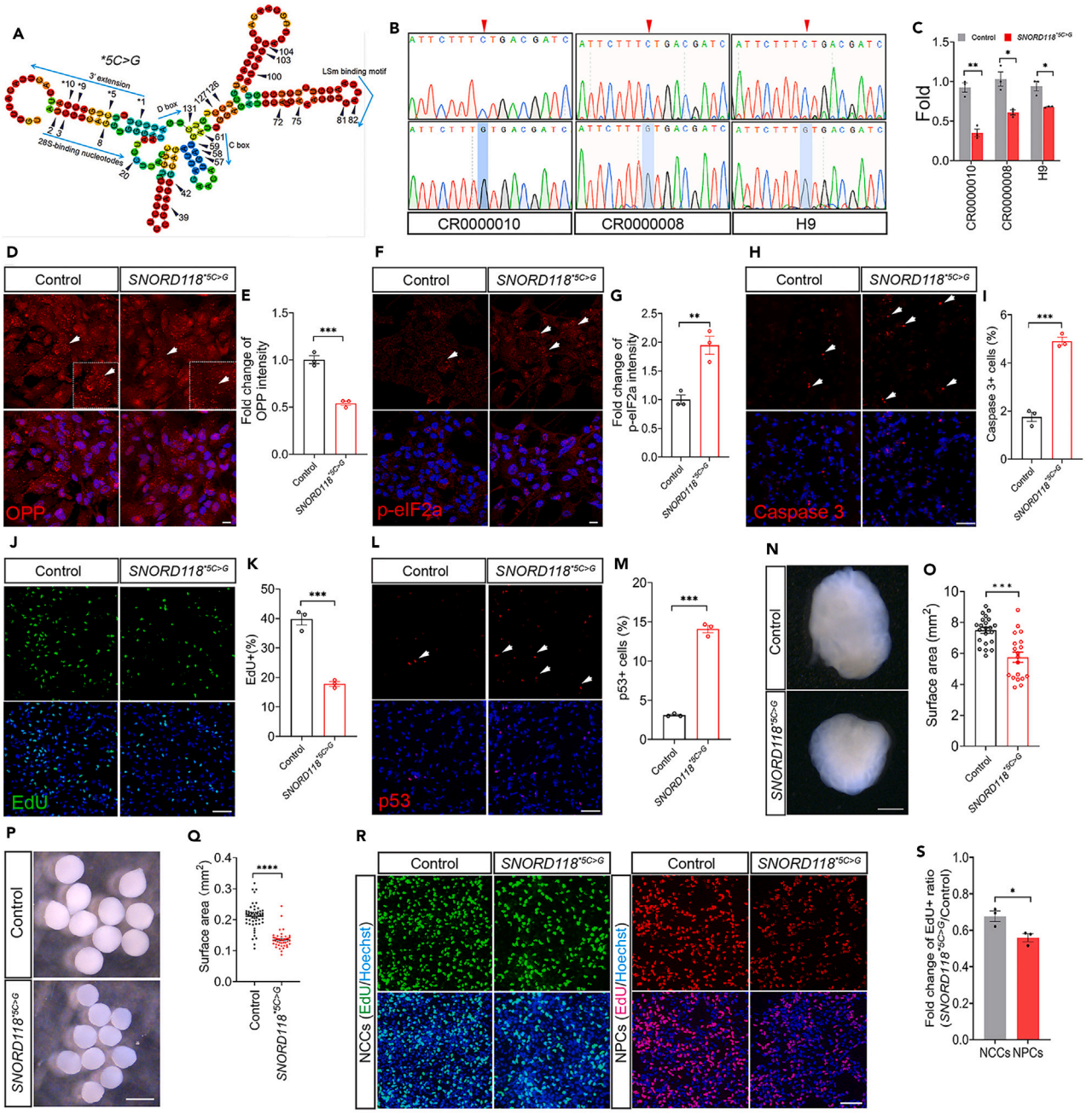

Figure 1. *SNORD118* mutations cause ribosomopathy hallmark defects leading to reduced organoid growth

(A) Diagram of *SNORD118* mutations in patients.

(B) Sanger sequencing analysis of the *SNORD118*$^{*5C>G}$ point mutation generated via CRISPR-Cas9 with ssODN. Three independent homozygous human pluripotent stem cell (hPSC) mutant lines have been generated. The top panels represent the reference genome and the bottom panels are point mutation lines. Red arrowheads indicate the mutation loci.

(C) qPCR analysis of snoRNA U8 levels in three hPSC lines, each represented by $n = 3$ distinct clones.

(C) qPCR analysis of U8 expression level in control and mutant hiPSCs.

(D) Representative images of OPP assay. Scale bar, 20 μm.

(E) Quantification of relative OPP intensity.

(F, H, J, and L) Immunofluorescent staining of p-eIF2α, caspase 3, EdU, and p53. Hoechst stains nuclei. Scale bars, 20 μm in F, 50 μm in (H, J, and L).

(G, I, K, and M) Quantification of the percentage of p-eIF2α-, caspase 3-, EdU-, and p53-positive cells.

(N) Bright-field images of control and *SNORD118*$^{*5C>G}$ cerebral organoids at 8 weeks. Scale bar, 1 mm.

(O) Quantification of surface areas of cerebral organoids. The $n = 26–30$ organoids from 3 independent lines.

Figure 1. *Continued*

(P) Bright-field images of neural crest organoids at day 21. Scale bar, 500 μm.

(Q) Quantification of the surface area of neural crest organoids at day 21. N = 54-45 organoids from 3 independent lines.

(R) EdU assay of hPSC-derived neural crest cells (NCCs) and neural progenitor cells (NPCs). Scale bar, 100 μm.

(S) Quantification of the percentage change of EdU^+ cells in mutant cells over controls between NCCs and NPCs. All data are represented as mean ± SEM calculated by Student's t test, $*p < 0.05$, $**p < 0.01$, $***p < 0.001$, $****p < 0.0001$.

family of small nucleolar RNAs (snoRNAs), which are a class of small RNA molecules that guide chemical modifications of rRNAs.[13–15] We recently developed a noncoding RNA target identification approach named psoralen analysis of RNA interactions and structures (PARIS), a psoralen crosslinking-based method for high-throughput mapping of RNA duplexes in living cells at genome-wide levels with near base-pair resolution.[16] Using the PARIS method, we found that U8 specifically binds to the 28S ribosomal RNA (rRNA).[16,17] Consistently, cell culture studies showed that U8 loss-of-function disrupts the cleavage of pre-rRNA and rRNA processing, leading to a ribosome biogenesis defect.[18,19] Here we developed a human iPSC/cerebral organoid model of *SNORD118* brain ribosomopathy. Our mutant iPSC-derived neural progenitor cells (NPCs) recapitulated the ribosomopathy hallmark defects and exhibited aberrant phase separation and nucleolar dysfunctions. Using LLPS effector fibrillarin (FBL) with depleted (loss of function) or an unrelated protein-swapped (gain-of-function) IDRs, we showed that LLPS is functionally important and its dysregulation contributes to ribosomopathy hallmark defects.

RESULTS

SNORD118 mutations cause ribosomopathy hallmark defects in hiPSC-derived NPCs and neural crest cells

Human genetics identified various *SNORD118* mutations in ribosomopathy patients (Figure 1A), who exhibited growth and mental retardation that specifically affect the brain but not other organs.[11,12] To establish a human model of *SNORD118* ribosomopathy, we used the CRISPR-Cas9 approach and generated three independent pluripotent stem cell (PSC) lines with homozygous *5C>G point mutations, which occur frequently in patient families.[11,12] DNA sequencing confirmed the homozygous *5C>G mutations (Figure 1B). Our qPCR analysis showed that there is a significant RNA downregulation of U8, encoded by *SNORD118*, in mutant PSCs compared to isogenic controls (Figure 1C), suggesting the loss of function of this homozygous point mutation.

SNORD118 deficiency is expected to disrupt ribosome biogenesis and protein synthesis, the main functions of nucleolus. Therefore, we performed an O-propargyl-puromycin (OPP) incorporation assay, in which OP-Puro acts as an analog of puromycin that enters the acceptor site of ribosomes and is incorporated into nascent polypeptides. OP-Puro can be detected by a click chemistry reaction to indicate protein synthesis.[20] Control and $SNORD118^{*5C>G}$ homozygous mutant human embryonic stem cells (ES) or iPSCs are differentiated into NPCs, marked by PAX6 and NESTIN (Figure S1A). There is a significant reduction in OPP intensity in mutant NPCs compared to isogenic controls (Figures 1D and 1E). Loss of ribosome biogenesis factors could impair the ribosomal assembly, leading to aberrant accumulation of orphan ribosomal proteins (RPs),[4,21] which elicits proteotoxic stress. Proteotoxic stress promotes the phosphorylation of eIF2 at serine 51 of the α subunit (eIF2α), triggering the integrated stress response.[22] Therefore, we used p-eIF2α to mark proteotoxic stress and found a significant increase in the p-eIF2α level in mutant NPCs compared to isogenic controls (Figures 1F and 1G). Therefore, *SNORD118* mutations trigger proteotoxic stress and disrupt nucleolar functions in protein synthesis.

The aberrant p53 signaling activation is a converging point of "ribosome stress" among different forms of ribosomopathies.[1,23] Therefore, we examined p53 activation and found an increased percentage of p53-positive cells in mutants compared to isogenic controls (Figures 1L and 1M). Sustained p53 activation leads to cell-cycle arrest and apoptosis. Therefore, we performed 5-ethynyl-2′-deoxyuridine (EdU) labeling to examine G1/S phase transition. *SNORD118* mutant NPCs exhibited a reduced percentage of EdU-positive cells (Figures 1J and 1K) as well as an increase in the percentage of apoptotic cells labeled by caspase 3 (Figures 1H and 1I). To investigate how impaired NPC behaviors affect brain growth, we generated cerebral organoids from $SNORD118^{*5C>G}$ homozygous mutant iPSCs coupled with isogenic controls. There was a significant size reduction of week 8 mutant cerebral organoids compared to controls (Figures 1N and 1O), recapitulating brain growth retardation in patients.

To investigate the cellular specificity of *SNORD118* functions, we generated neural crest cells (NCCs) from control and mutant iPSCs (Figure S2A). NCC identities are validated by the markers HNK1 and AP-2α (Figure S2B). $SNORD118^{*5C>G}$ homozygous mutant neural crest organoids are significantly smaller than controls (Figures 1P and 1Q). To investigate the mechanisms underlying smaller NCC organoid sizes, we performed immunostaining of NCC organoid sections. Similar to NPCs, mutant NCC organoids exhibited reduced cell proliferation as evidenced by EdU labeling (Figures S2C and S2D) as well as phosphohistone H3 (p-H3) staining (Figures S2E and S2F). Mutant NCC organoids also had an increase in cellular stress and cell death, as reflected by increased p53-and caspase 3-positive cells compared to controls (Figures S2G–S2J). Meanwhile, $SNORD118^{*5C>G}$ homozygous mutations caused a more pronounced cell proliferation reduction in NPCs than NCCs (Figures 1R and 1S). These results suggest that $SNORD118^{*5C>G}$ mutation does not solely affect neural cells while it has a more pronounced impact on NPCs compared to NCCs. Together, our iPSC-derived NPCs with *SNORD118* patient mutations exhibit the ribosomopathy-like hallmark defects and provide an *ex vivo* human cellular model for brain ribosomopathies.

Nucleolar morphology and LLPS are impaired in *SNORD118* mutant NPCs

To investigate mechanisms underlying ribosomopathy defects, we examined the morphology of the nucleolus, the site of ribosome biogenesis. This is because we observed that mutant NPCs exhibit abnormal nucleolar morphology, labeled by nucleophosmin (NPM1) staining, in our p-eIF2α-mediated proteotoxic stress studies (Figures 2A and 2B). The "core-shell"-like tripartite organization of the nucleolus consists of

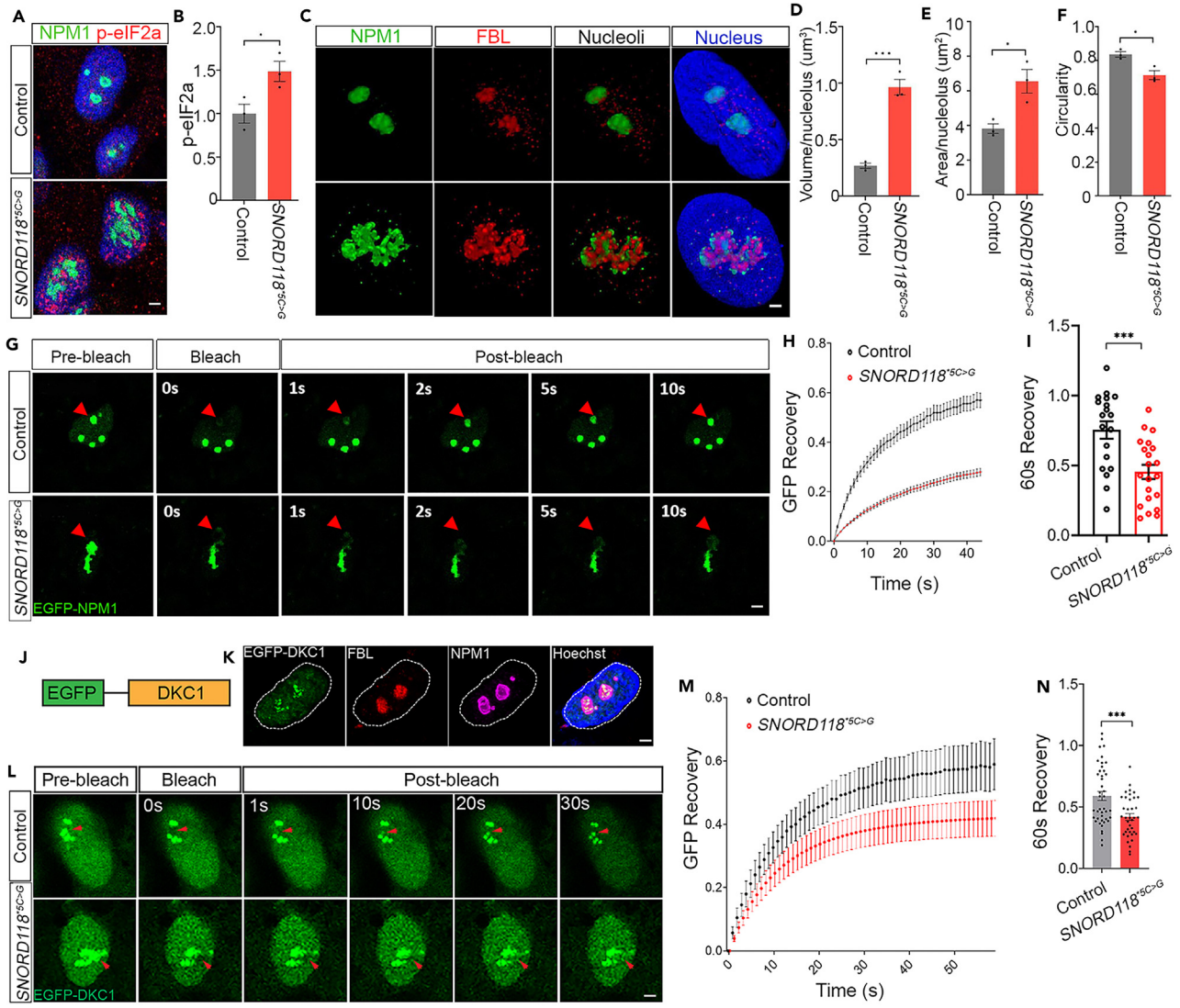

Figure 2. Nucleolar morphology and LLPS impairment in *SNORD118* mutant NPCs

(A) Confocal image of immunofluorescent staining of p-eIF2α staining in NPCs. Scale bars, 1 μm.

(B) Quantification of the fold change of p-eIF2α intensity.

(C) Representative images of NPM1 (green) and FBL (red) staining in control and *SNORD118*$^{*5C>G}$ homozygous mutant NPCs. Scale bar, 1 μm.

(D–F) Quantification of the volume of the nucleolus, the area of the nucleolus, and the nucleolar circularity. Three individual cell lines have been used for analysis, and about 800 cells in each cell line were analyzed.

(G) Representative images of GFP fluorescence recovery after photobleaching (FRAP) analysis. Red arrowheads represent spots with photo bleach. Scale bar, 1 μm.

(H) Line plots showing the dynamics of GFP recovery in each group.

(I) Quantification of the percentage of GFP intensity recovery in the 60 s of each group, *n* (control) = 39, *n* (*SNORD118*$^{*5C>G}$) = 39 cells.

(J) Diagram of *EGFP-DKC1* vector. (K) EGFP-DKC1 co-stained with FBL and NPM1 in NPCs. Scale bar, 1 μm.

(L) Representative images of FRAP analysis of EGFP-DKC1. Red arrowheads represent spots with photo bleach. Scale bar, 1 μm.

(M) Line plots showing the dynamics of EGFP recovery in each group.

(N) Quantification of the percentage of EGFP intensity recovery in the 60 s of each group, *n* = 42-39 cells. All data are represented as mean ± SEM calculated by Student's t test. Ns represents not significant, *$p < 0.05$, ***$p < 0.001$.

the inner FC labeled by RNA polymerase 1E, the DFC labeled by FBL, and the GC labeled by NPM1.[10] Control NPCs exhibited NPM1- and FBL-marked "core-shell"-like nucleolar morphology within the nucleus. In contrast, NPM1 and FBL proteins showed abnormal distribution and twisted morphology with aggregated patterns in the nucleolus, resulting in an appearance of expanded and "fragmented nucleoli" (Figure 2C). Statistical analysis revealed that there is a significant increase in the volume and area of the nucleolus and a decrease in the circularity

of nucleoli in mutant NPCs compared to isogenic controls (Figures 2D–2F, S1B, and S1C). These results suggest that *SNORD118* mutations lead to abnormal nucleolar structure, which is consistent with impaired nucleolar functions.

Nucleoli are membrane-less organelles that are organized by LLPS of their molecular components.[9,10] We hypothesized that impaired nucleolar structure is due to LLPS disruption in *SNORD118* mutant NPCs. To test this hypothesis, we directly measured LLPS properties. To this end, we examined the liquid-like dynamics of the nucleolar sub-compartments using fluorescence recovery after photobleaching (FRAP) assay on hiPSC-derived NPCs, in which the nucleolus was labeled by GFP-NPM1. NPM1 in control NPCs exhibited fast dynamics with nearly complete recovery within 10 s, consistent with the expected response for diffusion within a liquid. In contrast, NPM1 recovery in mutant NPCs is much slower (Figures 2G and 2H). Quantification at 60 s after photobleaching showed that the final recovery of NPM1 in mutant NPCs failed to reach the same degree of recovery as control cells (Figure 2I).

NPM1 labels a general GC region of the nucleolus. To investigate liquid properties of the DFC region specific for rRNA processing, we constructed a DFC marker DKC1 reporter (Figure 2J) and performed FRAP assays on NPCs. DKC1 is a subunit of the H/ACA ribonucleoprotein complex and is localized to the DFC of nucleoli.[10,13] Indeed, EGFP-DKC1 is specifically co-localized with FBL and is within more focused regions of NPM1-marked GC in the nucleolus (Figure 2K). The FRAP assay revealed that EGFP-DKC1 recovery is slower in mutant NPCs than in control cells (Figures 2L and 2M). Quantification at 60 s post-photobleaching indicated that the final recovery level of EGFP-DKC1 is lower in mutant NPCs compared to controls (Figure 2N). Together, LLPS properties of rRNA processing occurring DFC and ribosome assembly occurring GC are both impaired by the *SNORD118*$^{*5C>G}$ mutations, leading to disorganized nucleolar sub-compartments in iPSC-derived NPCs.

Nucleolar chaperone properties and nuclear degradation are defective in *SNORD118* mutant NPCs

The causes of proteotoxic stress in ribosomopathies are not clear. The LLPS defect in our mutant NPCs points us toward two LLPS-dependent nucleolar functions in proteostasis, including nucleolar chaperone and nuclear degradation.[24,25] The nucleolus functions as a phase-separated protein quality control compartment with chaperone-like properties, which reversibly stores misfolded proteins under stress.[25] Therefore, we hypothesized that LLPS impairment disrupts nucleolar chaperone functions and leads to proteotoxic stress in *SNORD118* mutant NPCs. To test this hypothesis, we examined the chaperone-like property of the nucleolus by monitoring how heat stress (HS) changes the fate of a nuclear reporter. This reporter is a fusion protein of the thermolabile firefly luciferase and heat-stable green fluorescent protein (GFP) carrying an N-terminal nuclear localization signal (NLS-LG). NLS-LG was diffusely distributed in the nucleus under normal conditions (Figure 3A). Upon HS incubation, a fraction of NLS-LG entered the nucleolus (labeled by NPM1) to store misfolded NLS-LG proteins, which were redistributed to the nucleoplasm in a diffused pattern upon HS recovery (Figure 3A). Compared to isogenic control NPCs, *SNORD118*$^{*5C>G}$ mutant NPCs displayed a significant increase in the percentage of nucleolus-remaining NLS-LG foci (Figures 3A and 3B). These results suggest that nucleolar chaperone-like function is compromised in mutant NPCs, which could contribute to proteotoxic stress.

Impaired ribosome biogenesis might lead to an imbalanced accumulation of orphan RPs,[4,21] which places an unusually heavy burden on the protein degradation machinery contributing to the proteotoxic stress. The ubiquitin-proteasome system (UPS) is a major proteolytic machine that selectively degrades ubiquitylated proteins. Unassembled orphan RPs that fail to incorporate into ribosomes are degraded by the UPS in the nucleoplasm.[24,26] To probe nuclear degradation in *SNORD118* mutant NPCs, we examined proteasome function under a hyperosmotic condition, which has been established to monitor proteasome-mediated degradation of orphan RPs.[24] To this end, we expressed PSMB2 (particle subunit proteasome subunit β type-2)-tdTomato to label the proteasome. Consistent with previous studies,[24] the PSMB2-labeled proteasomes were mainly observed in the nucleoplasm (Figure 3C). We found a significant decrease in PSMB2-labeled proteasomes in *SNORD118*$^{*5C>G}$ mutant NPCs compared to controls (Figures 3C and 3D). Hyperosmotic stress generates orphan RPs such as RPL29 that are degraded by UPS.[24] Therefore, we used RPL29-GFP to monitor orphan RP degradation. The majority of RPL29 proteins are co-localized into PSMB2-labeled proteasomes in control NPCs, while more RPL29 proteins are not co-localized with PSMB2 in mutant NPCs (Figures 3C and 3E), suggesting impaired orphan RP degradation. Together, these results suggest that impaired LLPS compromises nucleolar chaperone properties and nuclear degradation, which might collectively contribute to proteotoxic stress in *SNORD118*$^{*5C>G}$ mutant NPCs.

Ribosome biogenesis and *FBL* mRNA translation are compromised in mutant NPCs

To investigate the molecular mechanisms underlying the impaired LLPS in mutant NPCs, we focused on a well-established LLPS effector FBL that drives phase separation via its IDR motif.[9,10] Western blot (WB) analysis showed that there is a significant downregulation of FBL in *SNORD118*$^{*5C>G}$ mutant NPCs compared to isogenic controls (Figures 4A and 4B). To investigate the mechanism underlying FBL downregulation, we hypothesized that *SNORD118* mutations lead to impaired ribosome biogenesis and affect *FBL* mRNA translation. To test this hypothesis, we measured 28S and 18S rRNA using RNA screen tape analysis since *SNORD118* regulates rRNA processing.[18,19] There is a significant downregulation of the 28S/18S ratio (Figures 4C and 4D). To reinforce the connection between *SNORD118* and ribosome biogenesis, we used an actinomycin D (ActD)-based pharmacological approach. Protein synthesis is regulated by rRNA transcription or rRNA processing. ActD is an rRNA transcription inhibitor and disrupts ribosome biogenesis starting at the rRNA transcription level.[10] To measure RNA synthesis, we performed 5-ethynyluridine (5-EU) incorporation assay and found that mutant NPCs showed reduced 5-EU incorporation, which was further decreased after ActD treatment (Figures S1D and S1E). To measure protein synthesis, we conducted the OPP assay. The results indicated that mutant NPCs exhibited less OPP labeling, which was further reduced by ActD treatment (Figures 4E and 4F). These findings reinforce that *SNORD118*$^{*5C>G}$ mutant NPCs are more vulnerable to the disruption of ribosome biogenesis compared to controls.

We performed *SNORD118*-encoded U8 RNA pull-down to examine its interacting proteins. U8 belongs to C/D box snoRNAs that bind to proteins FBL, NOP56, and NOP58 for ribosome biogenesis. The second category of snoRNA is H/ACA box snoRNAs that bind to proteins

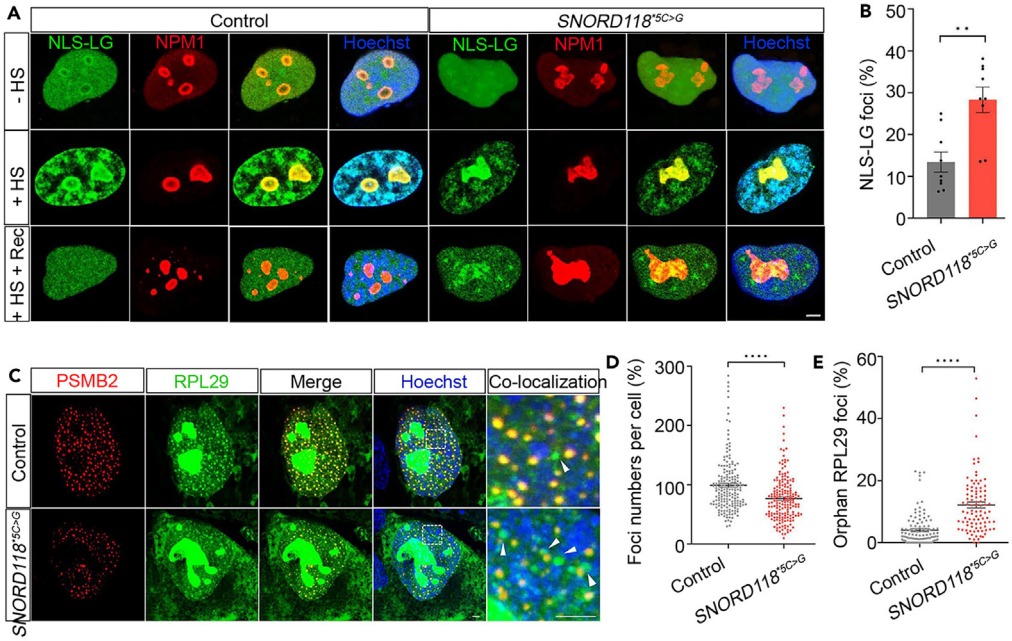

Figure 3. Impaired nucleolar chaperone properties and nuclear degradation in *SNORD118* mutant NPCs

(A) Immunofluorescent staining of NPCs transfected with NLS-LG (green) with antibodies against NPM1 (red). HS, heat shock at 42°C for 2 h. Rec, recovery at 37°C for 1 h. Scale bar, 5 μm.

(B) Quantification of the percentage of NLS-GFP foci within the nucleoli of NPCs at the recovery stage.

(C) Immunofluorescent staining of NPCs transfected with PSMB2-tdTomato and RPL29 plasmids. White arrowheads represent RPL29 proteins that are not localized to PSMB2-labeled proteasome foci. Scale bar, 1 μm.

(D and E) Quantification of the proteasome foci per cell and the percentage of orphan RPL29 foci. $N = 182$ cells (control) and 178 cells (*SNORD118*$^{*5C>G}$) in (D) and $N = 105$ cells (control) and 96 cells (*SNORD118*$^{*5C>G}$) in (E). All data are represented as Mean ± SEM calculated by Student's t-test, $^{**}p < 0.01$, and $^{****}p < 0.0001$.

DKC1, NOP10, and NHP2.[13] Our U8 pull-down followed by WB was carried out to examine the physical interaction between U8 and core components of nucleolar machinery. Indeed, U8 physically binds to the nucleolar protein FBL but does not bind to H/ACA ribonucleoprotein complex subunit DKC1 (Figures 4G and 4H), suggesting the specificity of U8 interactions with proteins. Although we doubled the protein loading from mutant NPCs, U8 still exhibited reduced binding to FBL (Figures 4G and 4H), suggesting the potential impairment of U8-FBL interaction in mutant NPCs compared to controls. 28S rRNA maturation is crucial for the assembly of the 80S ribosome. To monitor ribosomal assembly, we performed polysome profiling and found that both control and mutant NPCs exhibited typical peaks for the 40S, 60S, and 80S ribosomal subunits (Figure 4I). However, there was a notable reduction in the peak area corresponding to the 80S in mutant NPCs compared to controls (Figures 4I and 4J), suggesting that ribosome assembly is impaired in mutant NPCs. To determine how impaired ribosome assembly affects *FBL* mRNA translation, we isolated polysome followed by quantitative reverse-transcription PCR (RT-qPCR) analysis of *FBL*. There is a significant downregulation of *FBL* mRNA in polysome in mutant NPCs compared to controls (Figure 4K), suggesting an impaired *FBL* mRNA translation. Therefore, *SNORD118*$^{*5C>G}$ mutant NPCs exhibit impaired rRNA processing and ribosomal assembly, which disrupt protein synthesis and *FBL* mRNA translation.

Phase separation effector FBL rescues nucleolar morphology and LLPS defects of mutant NPCs

To test if phase separation effector FBL downregulation mediates nucleolar morphology and LLPS defects, we attempted to overexpress FBL to rescue these defects in mutant NPCs. We firstly used the PiggyBac method and generated stable *SNORD118*$^{*5C>G}$ hiPSC lines that express genes encoding full-length FBL followed by their differentiation into NPCs (Figure 5A). Ectopic FBL expression rescued the nucleolar morphology and LLPS defects in mutant NPCs (Figures 5C and 5D). These results suggest that *SNORD118* mutations disrupted nucleolar morphology and LLPS, at least in part, due to reduced levels of LLPS effector FBL.

Full-length FBL consists of two domains: an N-terminal arginine (R)/glycine (G)-rich domain with IDR and an RNA methyltransferase domain (MD). R/G IDR domain is responsible for LLPS and MD domain can methylate substrate rRNAs.[9] We hypothesized that the loss of FBL phase separation function drives the ribosomopathy-like defects in mutant NPCs. To test this hypothesis, we generated IDR-depleted FBL (FBL-C) that lacks the N-terminal fragment containing R/G IDR. In parallel, we generated a chimeric FBL in which its endogenous IDR was replaced by a different phase separation motif from an unrelated protein named nucleolin (Chimera FBL). Nucleolin is an RNA-binding protein with glycine arginine-rich IDR, which can replace FBL's IDR to form liquid droplet *in vitro*.[27,28] IDR deletion or replacement did not affect FBL cellular localization, as indicated by their co-localization with DFC marker DKC1 and GC marker NPM1 (Figure 5B). In contrast to full-length FBL, FBL

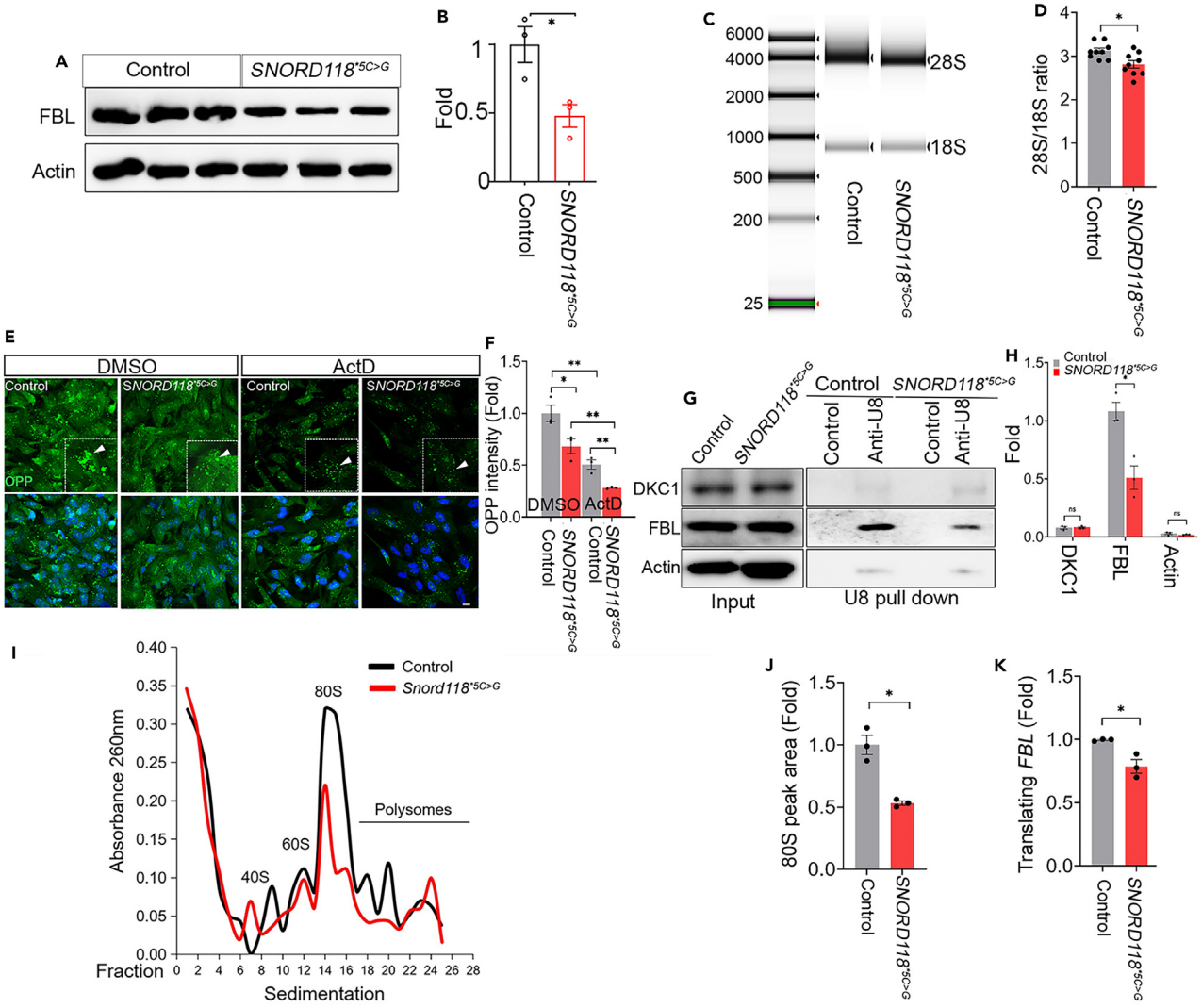

Figure 4. Ribosome biogenesis and *FBL* mRNA translation are compromised in mutant NPCs

(A) Western blot (WB) analysis of FBL protein levels.

(B) Quantification of WB results. $N = 3$.

(C) RNA screen tape analysis for the 28S and 18S rRNA biogenesis.

(D) Quantification of 28S/18S ratio. $N = 9$ samples from 3 hPSC-derived NPCs.

(E) OPP assay of control and *SNORD118*$^{*5C>G}$ mutant NPCs following treatment with DMSO or ActD (100 ng/mL) for 24 h. Scale bar, 20 μm.

(F) Fold change of OPP intensity. $N = 3$.

(G) Interaction profiles of snoRNA U8 with protein FBL, DKC1, and β-Actin in control and mutant NPCs.

(H) Quantification of U8-binding proteins. $N = 3$.

(I) Representative polysome profiles of Control and *SNORD118*$^{*5C>G}$ mutant NPCs.

(J) Fold change of assembled 80S ribosome peak area. $N = 3$.

(K) Fold change of translating *FBL* mRNA from polysomes, as determined by qPCR. $N = 3$. All data are represented as mean ± SEM calculated by Student's t test. The ns, no signification, $^{*}p < 0.05$.

lacking phase separation activity (FBL-C) failed to rescue LLPS properties and nucleolar morphology defects in mutant NPCs (Figures 5C and 5D). Remarkably, FBL chimeric proteins containing a phase separation motif from an unrelated nucleolin protein were sufficient to rescue nucleolar morphology and LLPS defect NPCs (Figures 5C–5G). These results demonstrated that the phase separation activity of FBL is essential to prevent nucleolar morphology and LLPS defects in *SNORD118*$^{*5C>G}$ mutant NPCs. Through these studies, we functionally confirmed a set of molecular tools that specifically promote (full-length FBL and chimeric FBL) or inhibit (FBL-C) nucleolar LLPS activity, which allows us to investigate functions of phase separation in ribosomopathy defects.

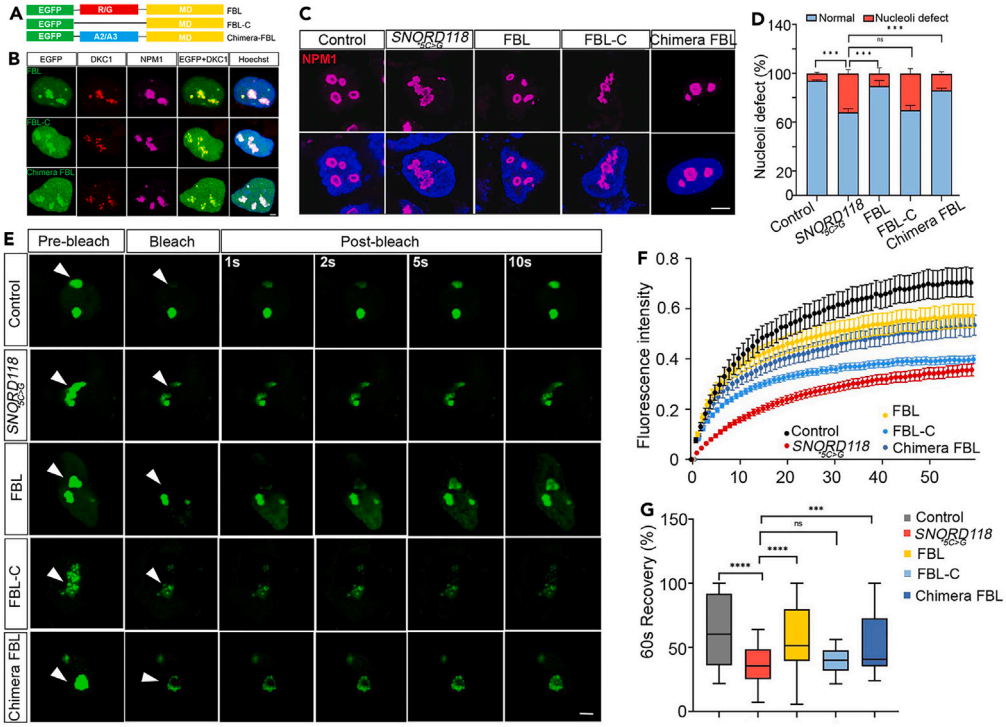

Figure 5. FBL rescues nucleolar morphology and LLPS defects of mutant NPCs in a phase separation motif-dependent manner

(A) Diagram of wild type (FBL), IDR-depleted (FBL-C) mutant, and chimeric FBL, in which the intrinsic IDR is replaced by another LLPS motif from an unrelated protein.

(B) Immunostaining of different EGFP-FBL isoforms for their co-localization with DKC1 and NPM1 in NPCs. Scale bar, 1 μm.

(C) Representative images of NPM1 staining in control and *SNORD118*$^{*5C>G}$ NPCs with or without the expression of FBL, FBL-C, or chimeric FBL. Scale bar, 5 μm.

(D) Quantification of the percentage of intact and disrupted nucleolar morphology.

(E) Representative images of GFP fluorescence recovery after photobleaching (FRAP) analysis. White arrowheads represent spots with photo bleach. Control and *SNORD118*$^{*5C>G}$ NPCs were labeled with GFP-tagged NPM1, while the rest of the NPCs were visualized using various forms of EGFP-fused FBL. Scale bar, 2 μm.

(F) Line plots showing the dynamics of GFP recovery in each group.

(G) Quantification of the percentage of GFP intensity recovery in the 60 s of each group, *n* (control) = 39, *n* (*SNORD118*$^{*5C>G}$) = 39, *n* (FBL) = 35, *n* (FBL-C) = 38, *n* (Chimeric FBL) = 37 cells. All data are represented as mean ± SEM calculated by Student's t test, *$p < 0.05$, ***$p < 0.001$, ****$p < 0.0001$, ns, not significant.

Phase separation activity is essential to mitigate ribosomopathy hallmark defects in mutant NPCs

To test the hypothesis that phase separation impairment drives ribosomopathy defects in mutant NPCs, we focused on these hallmark cellular defects in *SNORD118*$^{*5C>G}$ mutant NPCs. Using the PiggyBac method, we generated control and *SNORD118*$^{*5C>G}$ homozygous mutant hiPSC lines that express genes encoding full-length FBL, IDR-deleted FBL (FBL-C), and chimeric FBL with swapped IDR from nucleolin followed by inducing their differentiation into NPCs. To investigate the role of LLPS in protein synthesis, we performed an OPP assay and found that LLPS activation by FBL or chimeric FBL rescued protein synthesis loss in mutant NPCs, whereas FBL lacking phase separation activity failed to do so (Figures 6A and 6B). We used immunostaining of p-eIF2α and p53 to monitor proteotoxic stress and p53 activation. Quantification data showed that full-length FBL and chimeric FBL can mitigate proteotoxic stress and p53 activation, both of which cannot be reduced by IDR-deleted FBL-C (Figures 6C–6F). These results suggest that phase separation impairment in *SNORD118* mutant NPCs is causatively linked with ribosomopathy hallmark defects, including protein synthesis loss, proteotoxic stress, and p53 activation.

To investigate the effects of phase separation changes on cellular behaviors, we performed EdU labeling and cleaved caspase 3 staining to measure NPC proliferation and survival, respectively. LLPS promotion by full-length or chimeric FBL can significantly reduce defects in cell proliferation and cell survival of mutant NPCs. In contrast, FBL lacking phase separation activity (FBL-C) cannot mitigate cell proliferation and survival defects in mutant NPCs (Figures 6G–6J). Together, these results suggest that impaired phase separation activities contribute to ribosomopathy hallmark defects, which can be mitigated by LLPS promotion in *SNORD118*$^{*5C>G}$ mutant NPCs.

Phase separation promotion partially rescues neural cell fate and organoid growth in mutant cerebral organoids

To investigate the functional significance of LLPS in brain development, we turned to our cerebral organoid models. We induced control and *SNORD118* mutant iPSCs with or without ectopic expression of FBL into cerebral organoids. Mutant iPSCs with the expression of FBL lacking phase separation activity can be differentiated into NPCs but fail to form mature cerebral organoids. Therefore, FBL lacking phase separation

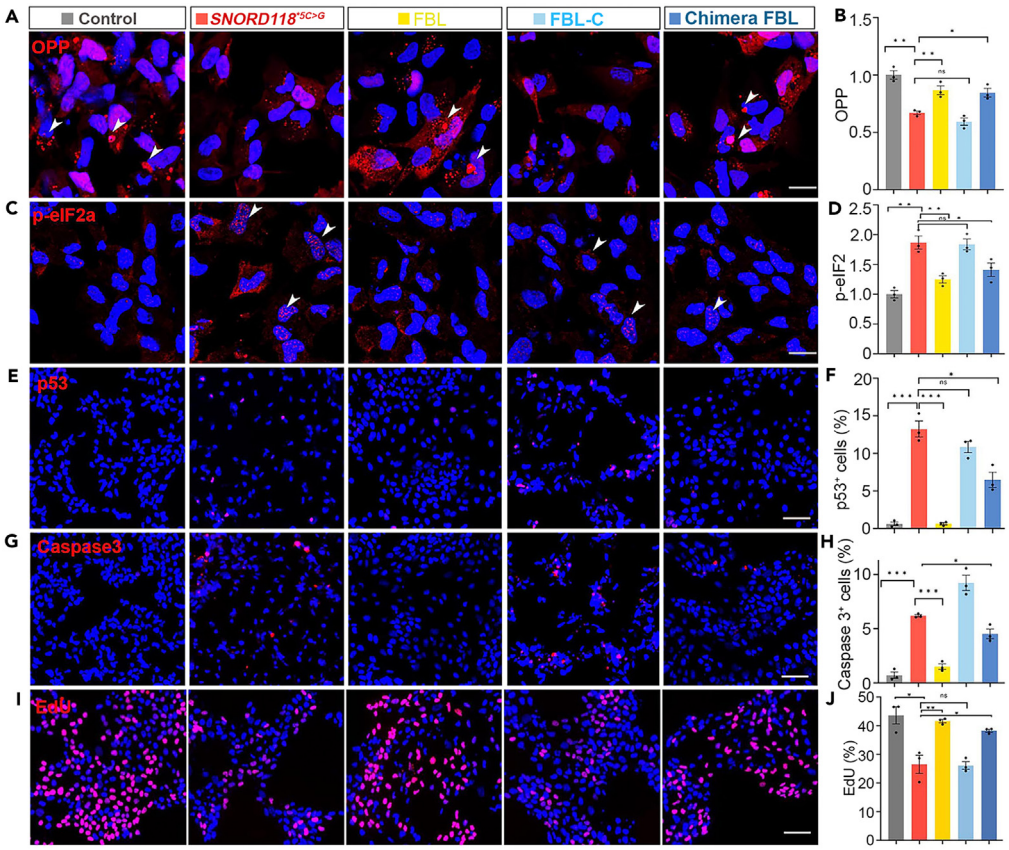

Figure 6. LLPS of FBL is required for rescuing ribosomopathy hallmark defects in mutant NPCs

(A) Representative images of OPP assay in control and *SNORD118*$^{*5C>G}$ mutant NPCs with or without FBL, FBL-C, or Chimeric FBL. White Arrowheads indicate OPP incorporated in the cells. Scale bar, 20 μm.

(B) Quantification of relative OPP intensity.

(C, E, G, and I) Immunofluorescent staining of p-eIF2α, p53, Caspase 3, and EdU. White Arrowhead indicated the positive signals of p-eIF2α. Scale bar, 20 μm in (C), 50 μm in (E, G, and I).

(D, F, H, and J) Quantification of the percentage of OPP-, p-eIF2α-, p53-, caspase 3-, or EdU positive cells. All data are represented as mean ± SEM calculated by Student's t test, *$p < 0.05$, **$p < 0.01$, ***$p < 0.001$, ****$p < 0.0001$.

activity is not included in our cerebral organoid studies. Surface area measurement showed that full-length FBL and chimeric FBL can significantly rescue the sizes of *SNORD118* mutant cerebral organoids (Figures 7A and 7B). These results suggest that phase separation activity of FBL is important for cerebral organoid growth.

To examine ribosomopathy hallmark defects in cerebral organoids, we focused on p53 activation and cell death. Full-length and chimeric FBL can significantly rescue the p53 activation and cell death defects in mutant NPCs marked by SOX2 in cerebral organoids (Figures 7C–7F and S1F). To investigate the cellular mechanisms underlying the increased organoid size by LLPS promotion, we used Ki67 to label all cycling cells and BrdU to mark G1/S phase transition NPCs in the ventricular zone/subventricular zone (VZ/SVZ)-like cortical regions in the organoids. Immunohistochemistry staining showed that mutant organoids exhibited a decrease of BrdU- and Ki67-positive cells, which were significantly rescued by full-length or chimeric FBL (Figures 7G, 7H, and S1F). In parallel, we used p-H3 staining to label mitotic NPCs marked by SOX2 and found that LLPS promotion can significantly increase the percentage of p-H3-positive NPCs, which are reduced in mutants compared to control organoids (Figures 7I, 7J, and S1F). To further investigate the functional significance of LLPS promotion in cerebral organoids, we examined neuronal production and found that full-length or chimeric FBL significantly rescued the reduction of CTIP2- and TBR1-positive neurons in mutant cerebral organoids (Figures 7K–7N and S1F). Together, these results suggest that phase separation activity is functionally important for the restoration of neuronal cell fate and growth defects in *SNORD118* mutant cerebral organoids.

DISCUSSION

Utilizing our human iPSC-derived NPC and cerebral organoid models of *SNORD118* ribosomopathies, we identified impaired phase separation and nucleolar functions in mutant NPCs and organoids. Further mechanistic studies suggest that nucleolar LLPS dysfunction contributes to ribosomopathy hallmark phenotypes, including protein synthesis loss, p53 activation, and proteotoxic stress (Figure 8).

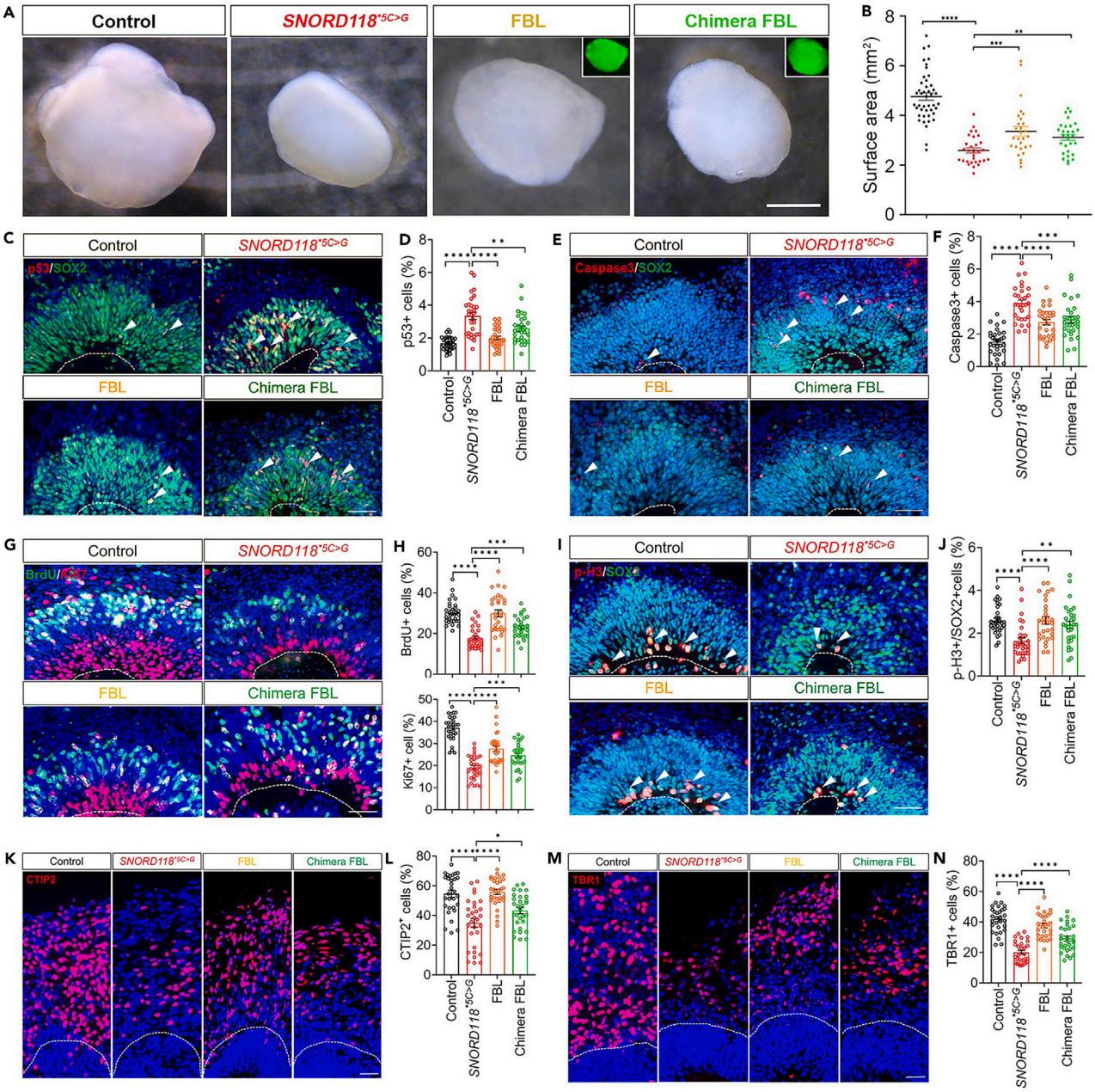

Figure 7. LLPS promotion rescues neural cell fate and growth in mutant cerebral organoids

(A) Bright-field images of 8-week control and *SNORD118*$^{*5C>G}$ cerebral organoids with or without the expression of FBL or chimeric FBL. Scale bar, 1 mm.

(B) Quantification of organoid surface areas. *N* = 28–44 organoids from 3 independent batches.

(C and E) Immunofluorescent staining of SOX2 (green) together with p53 (red) or caspase 3 (red) in cerebral organoids. Scale bar, 50 μm.

(D and F) Quantification of the percentage of p53-or caspase 3-positive NPCs marked by SOX2 in the cerebral organoids. *N* = 24–36 cortex-like structures from 12 organoids in each group.

(G and I) Immunofluorescent staining of BrdU (green) and Ki67 (red) as well as p-H3 (red) and SOX2 (green) positive cells in cerebral organoids. Scale bar, 50 μm.

(H and J) Quantification of the percentage of BrdU-, Ki67,- or p-H3; SOX2-positive cells in the cerebral organoids. *N* = 24–36 cortex-like structures from 12 organoids in each group.

(K and M) Immunofluorescent staining of CTIP2 and TBR1 in cerebral organoids. Scale bar, 50 μm.

(L and N) Quantification of the percentage of CTIP2- or TBR1-positive cells. *N* = 30–36 cortex-like structures from 12 organoids in each group. All data are represented as mean ± SEM calculated by one-way ANOVA with Tukey post hoc tests or Student's t test, *$p < 0.05$, **$p < 0.01$, ***$p < 0.001$, ****$p < 0.0001$.

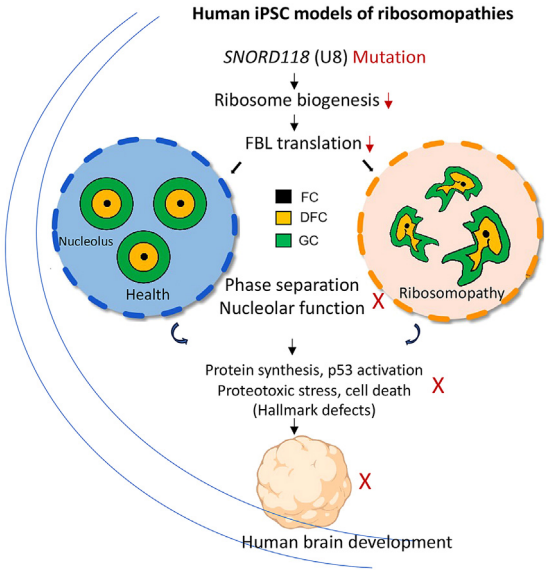

Figure 8. Schematic of impaired phase separation and nucleolar functions leading to brain ribosomopathies

Human iPSC-derived cell and organoid models are coupled with CRISPR genome editing to study human brain-related ribosomopathies caused by mutations in ribosome biogenesis factor non-coding RNA *SNORD118*-encoded U8. *SNORD118* mutations disrupt ribosome biogenesis and mRNA translation of phase separation effector FBL, which disturbs the phase separation and nucleolar functions. Impaired phase separation and nucleolar functions cause ribosomopathy-like hallmark defects, including protein synthesis deficiency, p53 activation, proteotoxic stress, and cell death, which collectively contribute to brain developmental delay.

Our findings provide mechanistic insights into the pathogenesis of ribosomopathies. First, it has been established that "ribosome stress" converges on the p53 signaling, resulting in cell-cycle arrest and apoptosis.[23,29,30] However, it remains poorly understood how p53 signaling is activated. We showed that the impairment of LLPS-mediated nucleolar organization drives p53 activation. This is supported by findings that FBL-mediated LLPS promotion rescued p53 activation,[9] while FBL with deleted IDR (LLPS motif) failed to do so. Moreover, the p53 overactivation defect is also rescued by a chimeric FBL, in which the endogenous IDR is swapped with another IDR from an unrelated protein nucleolin, suggesting the specific requirement of phase separation in regulating p53 signaling. Second, the causes of proteotoxic stress in ribosomopathies have been unclear. Our results suggest that the disruption of LLPS-dependent nuclear degradation of orphan RPs could contribute to this proteotoxic stress. RPs are produced at high levels beyond what is required for the typical rate of ribosome-subunit generation and are accumulated in the nucleolus; there is a continual degradation of unassembled RPs in the nucleoplasm.[26] *SNORD118* mutations might yield an accumulation of orphan RPs that are not incorporated into functional ribosomal units,[4,21] which in turn overloads the degradation machine, including the proteasome in the nucleus. In parallel, proteasomal degradation in mutant NPCs could not function efficiently due to LLPS impairment since LLPS is required for the formation of a nuclear proteolytic compartment that promotes proteasomal degradation.[24] Third, we found impaired chaperone properties of the nucleolus in *SNORD118* mutant NPCs. The nucleolus exhibits chaperone-like properties and functions as an LLPS-dependent quality control compartment.[25] Therefore, *SNORD118* mutation-associated LLPS impairment compromises the chaperone-like properties as well as the misfolded protein storage capacities of the nucleolus. Together, orphan RP accumulation, nuclear degradation disruption, and impaired nucleolar chaperone function might collectively contribute to proteotoxic stress in ribosomopathies.

Our functional study of LLPS in brain development is significant. LLPS has been increasingly implicated in a wide range of biological processes.[31,32] However, it is challenging to establish the causative relationship between LLPS and its functional significance. By deleting endogenous IDR or adding IDR from an unrelated protein nucleolin, we generated LLPS-defective or -promotion versions of FBL and functionally demonstrated that phase separation is required to mitigate proteotoxic stress in *SNORD118* mutant NPCs. As a biophysical principle of nucleolus organization, LLPS has been recognized in promoting ribosome biogenesis and protein synthesis functions.[10] Here we add another layer of LLPS functions in nuclear protein degradation, nucleolar chaperone function, and p53 activation prevention. Remarkably, FBL with a phase separation motif from an unrelated protein can rescue defects in mutant NPC proliferation, survival, and neuronal production, suggesting the specificity and importance of LLPS functions in mitigating ribosomopathy hallmark defects. These results suggest that targeting LLPS to modulate nucleolar organization might be a therapeutic strategy for nucleolar dysfunction-associated diseases. Overall, our study highlights the importance of LLPS-mediated organization of the ribosome biogenesis compartment, rather than ribosome biogenesis *per se* in ribosomopathies.

Limitations of the study

Our studies suggest but have not demonstrated a feedback loop in which *SNORD118* mutation-mediated ribosome biogenesis disrupts *FBL* mRNA translation and nucleolar phase separation, which in turn impairs nucleolar organization and ribosome biogenesis. *SNORD118* mutations lead to a highly complex brain ribosomopathy in patients, including leukoencephalopathy, intracranial calcifications, cysts, seizures, and motor function decline. In addition to brain development, future studies should investigate phase separation in adult neuronal activity and brain functions. It is also important to understand why *SNORD118* mutation-induced disruption of global ribosome biogenesis selectively affects brain compared to other organs.

STAR★METHODS

Detailed methods are provided in the online version of this paper and include the following:

- KEY RESOURCES TABLE
- RESOURCE AVAILABILITY
  - Lead contact
  - Materials availability
  - Data and code availability
- EXPERIMENTAL MODEL AND STUDY PARTICIPANT DETAILS
- METHOD DETAILS
  - Human iPSC culture
  - Genome editing
  - Human neural progenitor cell (NPC) generation
  - Generation of cerebral organoids
  - Generation of neural crest organoids
  - Real-time quantitative PCR
  - Immunostaining
  - BrdU labeling and EdU assay
  - O- propargyl-puromycin (OPP) incorporation assay
  - Polysome profiling
  - RNA ScreenTape analysis
  - RNA-protein interaction assay
- QUANTIFICATION AND STATISTICAL ANALYSIS
  - Image analysis and quantification
  - Statistical analysis

SUPPLEMENTAL INFORMATION

Supplemental information can be found online at https://doi.org/10.1016/j.isci.2024.110430.

ACKNOWLEDGMENTS

We thank Chen's laboratory colleagues for stimulating discussions. We are grateful for Kimi Nakaki's critical reading of the manuscript. Chen laboratory is supported by funds from the Associate Dean of Research Fund from the Center for Craniofacial Molecular Biology, Herman Ostrow School of Dentistry at the University of Southern California, and grants R21AG075665 (J.C.) and R21AG070681 (J.C.) from the National Institutes of Health.

AUTHOR CONTRIBUTIONS

W.Z., M.J.Z., L.M., J.S., Q.C., and Z.Y.L. conceived and performed all experiments. Z.P.L. helped with the manuscript writing. J.-F.C. and W.Z. designed and interpreted the experiments and wrote the manuscript.

DECLARATION OF INTERESTS

The authors declare no competing interests.

Received: November 13, 2023
Revised: May 16, 2024
Accepted: June 28, 2024
Published: July 1, 2024

REFERENCES

1. Mills, E.W., and Green, R. (2017). Ribosomopathies: There's strength in numbers. Science *358*, eaan2755. https://doi.org/10.1126/science.aan2755.
2. Xue, S., and Barna, M. (2012). Specialized ribosomes: a new frontier in gene regulation and organismal biology. Nat. Rev. Mol. Cell Biol. *13*, 355–369. https://doi.org/10.1038/nrm3359.
3. Khajuria, R.K., Munschauer, M., Ulirsch, J.C., Fiorini, C., Ludwig, L.S., McFarland, S.K., Abdulhay, N.J., Specht, H., Keshishian, H., Mani, D.R., et al. (2018). Ribosome Levels Selectively Regulate Translation and Lineage Commitment in Human Hematopoiesis. Cell *173*, 90–103.e19. https://doi.org/10.1016/j.cell.2018.02.036.
4. Recasens-Alvarez, C., Alexandre, C., Kirkpatrick, J., Nojima, H., Huels, D.J., Snijders, A.P., and Vincent, J.-P. (2021). Ribosomopathy-associated mutations cause

proteotoxic stress that is alleviated by TOR inhibition. Nat. Cell Biol. *23*, 127–135. https://doi.org/10.1038/s41556-020-00626-1.

5. Yelick, P.C., and Trainor, P.A. (2015). Ribosomopathies: Global process, tissue specific defects. Rare Dis. *3*, e1025185. https://doi.org/10.1080/21675511.2015.1025185.
6. Pollen, A.A., Bhaduri, A., Andrews, M.G., Nowakowski, T.J., Meyerson, O.S., Mostajo-Radji, M.A., Lullo, E.D., Alvarado, B., Bedolli, M., Dougherty, M.L., et al. (2019). Establishing Cerebral Organoids as Models of Human-Specific Brain Evolution. Cell *176*, 743–756.e17. https://doi.org/10.1016/j.cell.2019.01.017.
7. Lancaster, M.A., Renner, M., Martin, C.-A., Wenzel, D., Bicknell, L.S., Hurles, M.E., Homfray, T., Penninger, J.M., Jackson, A.P., and Knoblich, J.A. (2013). Cerebral organoids model human brain development and microcephaly. Nature *501*, 373–379. https://doi.org/10.1038/nature12517.
8. Lullo, E.D., and Kriegstein, A.R. (2017). The use of brain organoids to investigate neural development and disease. Nat. Rev. Neurosci. *18*, 573–584. https://doi.org/10.1038/nrn.2017.107.
9. Feric, M., Vaidya, N., Harmon, T.S., Mitrea, D.M., Zhu, L., Richardson, T.M., Kriwacki, R.W., Pappu, R.V., and Brangwynne, C.P. (2016). Coexisting Liquid Phases Underlie Nucleolar Subcompartments. Cell *165*, 1686–1697. https://doi.org/10.1016/j.cell.2016.04.047.
10. Lafontaine, D.L.J., Riback, J.A., Bascetin, R., and Brangwynne, C.P. (2021). The nucleolus as a multiphase liquid condensate. Nat. Rev. Mol. Cell Biol. *22*, 165–182. https://doi.org/10.1038/s41580-020-0272-6.
11. Crow, Y.J., Marshall, H., Rice, G.I., Seabra, L., Jenkinson, E.M., Baranano, K., Battini, R., Berger, A., Blair, E., Blauwblomme, T., et al. (2021). Leukoencephalopathy with calcifications and cysts: Genetic and phenotypic spectrum. Am. J. Med. Genet. *185*, 15–25. https://doi.org/10.1002/ajmg.a.61907.
12. Jenkinson, E.M., Rodero, M.P., Kasher, P.R., Uggenti, C., Oojageer, A., Goosey, L.C., Rose, Y., Kershaw, C.J., Urquhart, J.E., Williams, S.G., et al. (2016). Mutations in SNORD118 cause the cerebral microangiopathy leukoencephalopathy with calcifications and cysts. Nat. Genet. *48*, 1185–1192. https://doi.org/10.1038/ng.3661.
13. Kiss, T., Fayet, E., Jády, B.E., Richard, P., and Weber, M. (2006). Biogenesis and Intranuclear Trafficking of Human Box C/D and H/ACA RNPs. Cold Spring Harb. Symp. Quant. Biol. *71*, 407–417. https://doi.org/10.1101/sqb.2006.71.025.
14. Stepanov, G.A., Filippova, J.A., Komissarov, A.B., Kuligina, E.V., Richter, V.A., and Semenov, D.V. (2015). Regulatory Role of Small Nucleolar RNAs in Human Diseases. BioMed Res. Int. *2015*, 206849. https://doi.org/10.1155/2015/206849.
15. Kufel, J., and Grzechnik, P. (2019). Small Nucleolar RNAs Tell a Different Tale. Trends Genet. *35*, 104–117. https://doi.org/10.1016/j.tig.2018.11.005.
16. Lu, Z., Zhang, Q.C., Lee, B., Flynn, R.A., Smith, M.A., Robinson, J.T., Davidovich, C., Gooding, A.R., Goodrich, K.J., Mattick, J.S., et al. (2016). RNA Duplex Map in Living Cells Reveals Higher-Order Transcriptome Structure. Cell *165*, 1267–1279. https://doi.org/10.1016/j.cell.2016.04.028.
17. Zhang, M., Li, K., Bai, J., Velema, W.A., Yu, C., van Damme, R., Lee, W.H., Corpuz, M.L., Chen, J.-F., and Lu, Z. (2021). Optimized photochemistry enables efficient analysis of dynamic RNA structuromes and interactomes in genetic and infectious diseases. Nat. Commun. *12*, 2344. https://doi.org/10.1038/s41467-021-22552-y.
18. Langhendries, J.-L., Nicolas, E., Doumont, G., Goldman, S., and Lafontaine, D.L.J. (2016). The human box C/D snoRNAs U3 and U8 are required for pre-rRNA processing and tumorigenesis. Oncotarget *7*, 59519–59534. https://doi.org/10.18632/oncotarget.11148.
19. McFadden, E.J., and Baserga, S.J. (2022). U8 variants on the brain: a small nucleolar RNA and human disease. RNA Biol. *19*, 412–418. https://doi.org/10.1080/15476286.2022.2048563.
20. Liu, J., Xu, Y., Stoleru, D., and Salic, A. (2012). Imaging protein synthesis in cells and tissues with an alkyne analog of puromycin. Proc. Natl. Acad. Sci. USA *109*, 413–418. https://doi.org/10.1073/pnas.1111561108.
21. Tye, B.W., Commins, N., Ryazanova, L.V., Wühr, M., Springer, M., Pincus, D., and Churchman, L.S. (2019). Proteotoxicity from aberrant ribosome biogenesis compromises cell fitness. Elife *8*, e43002. https://doi.org/10.7554/elife.43002.
22. Pakos-Zebrucka, K., Koryga, I., Mnich, K., Ljujic, M., Samali, A., and Gorman, A.M. (2016). The integrated stress response. EMBO Rep. *17*, 1374–1395. https://doi.org/10.15252/embr.201642195.
23. Sloan, K.E., Bohnsack, M.T., and Watkins, N.J. (2013). The 5S RNP Couples p53 Homeostasis to Ribosome Biogenesis and Nucleolar Stress. Cell Rep. *5*, 237–247. https://doi.org/10.1016/j.celrep.2013.08.049.
24. Yasuda, S., Tsuchiya, H., Kaiho, A., Guo, Q., Ikeuchi, K., Endo, A., Arai, N., Ohtake, F., Murata, S., Inada, T., et al. (2020). Stress- and ubiquitylation-dependent phase separation of the proteasome. Nature *578*, 296–300. https://doi.org/10.1038/s41586-020-1982-9.
25. Frottin, F., Schueder, F., Tiwary, S., Gupta, R., Körner, R., Schlichthaerle, T., Cox, J., Jungmann, R., Hartl, F.U., and Hipp, M.S. (2019). The nucleolus functions as a phase-separated protein quality control compartment. Science *365*, 342–347. https://doi.org/10.1126/science.aaw9157.
26. Lam, Y.W., Lamond, A.I., Mann, M., and Andersen, J.S. (2007). Analysis of Nucleolar Protein Dynamics Reveals the Nuclear Degradation of Ribosomal Proteins. Curr. Biol. *17*, 749–760. https://doi.org/10.1016/j.cub.2007.03.064.
27. Kim, E., and Kwon, I. (2021). Phase transition of fibrillarin LC domain regulates localization and protein interaction of fibrillarin. Biochem. J. *478*, 799–810. https://doi.org/10.1042/bcj20200847.
28. Doron-Mandel, E., Koppel, I., Abraham, O., Rishal, I., Smith, T.P., Buchanan, C.N., Sahoo, P.K., Kadlec, J., Oses-Prieto, J.A., Kawaguchi, R., et al. (2021). The glycine arginine-rich domain of the RNA-binding protein nucleolin regulates its subcellular localization. EMBO J. *40*, e107158. https://doi.org/10.15252/embj.2020107158.
29. Chakraborty, A., Uechi, T., and Kenmochi, N. (2011). Guarding the 'translation apparatus': defective ribosome biogenesis and the p53 signaling pathway. Wiley Interdiscip. Rev. RNA *2*, 507–522. https://doi.org/10.1002/wrna.73.
30. Badrock, A.P., Uggenti, C., Wacheul, L., Crilly, S., Jenkinson, E.M., Rice, G.I., Kasher, P.R., Lafontaine, D.L.J., Crow, Y.J., and O'Keefe, R.T. (2020). Analysis of U8 snoRNA Variants in Zebrafish Reveals How Bi-allelic Variants Cause Leukoencephalopathy with Calcifications and Cysts. Am. J. Hum. Genet. *106*, 694–706. https://doi.org/10.1016/j.ajhg.2020.04.003.
31. Alberti, S., Gladfelter, A., and Mittag, T. (2019). Considerations and Challenges in Studying Liquid-Liquid Phase Separation and Biomolecular Condensates. Cell *176*, 419–434. https://doi.org/10.1016/j.cell.2018.12.035.
32. McSwiggen, D.T., Mir, M., Darzacq, X., and Tjian, R. (2019). Evaluating phase separation in live cells: diagnosis, caveats, and functional consequences. Genes Dev. *33*, 1619–1634. https://doi.org/10.1101/gad.331520.119.
33. Zhang, W., Ma, L., Yang, M., Shao, Q., Xu, J., Lu, Z., Zhao, Z., Chen, R., Chai, Y., and Chen, J.-F. (2020). Cerebral organoid and mouse models reveal a RAB39b–PI3K–mTOR pathway-dependent dysregulation of cortical development leading to macrocephaly/autism phenotypes. Gene Dev. *34*, 580–597. https://doi.org/10.1101/gad.332494.119.
34. Zhang, W., Yang, S.-L., Yang, M., Herrlinger, S., Shao, Q., Collar, J.L., Fierro, E., Shi, Y., Liu, A., Lu, H., et al. (2019). Modeling microcephaly with cerebral organoids reveals a WDR62–CEP170–KIF2A pathway promoting cilium disassembly in neural progenitors. Nat. Commun. *10*, 2612. https://doi.org/10.1038/s41467-019-10497-2.

STAR★METHODS

KEY RESOURCES TABLE

REAGENT or RESOURCE	SOURCE	IDENTIFIER
Antibodies		
Rat-anti Sox2	Invitrogen	Cat# 14-9811-95; RRID: AB_2865466
Mouse-anti p53	Santa Cruz Biotechnology	Cat# sc-13580; RRID: AB_628088
Rabbit-anti Cleaved Caspase 3	Cell Signaling Technology	Cat# 9661; RRID: AB_2341188
Mouse-anti PAX6	DSHB	Cat# pax6; RRID: AB_528427
Rabbit-anti p-H3(Ser10)	Cell Signaling Technology	Cat# 9701; RRID: AB_331535
Rat-anti CTIP2	Abcam	Cat# ab18465; RRID: AB_2064130
Rabbit-anti TBR1	Abcam	Cat# ab31940; RRID: AB_2200219
Rat-anti BrdU	Abcam	Cat# ab6326; RRID: AB_305426
Mouse-anti Ki67	BD Biosciences	Cat# 550609; RRID: AB_393778
Mouse-anti SATB2	Abcam	Cat# ab51502; RRID: AB_882455
Mouse-anti HNK-1	DSHB	Cat# 3H5; RRID: AB_2314644
Mouse-anti AP-2α	DSHB	Cat# 3b5; RRID: AB_528084
Mouse-anti B23 (NPM1)	Sigma	Cat# B0556; RRID: AB_2154872
Rabbit-anti DKC1	Thermo Fisher Scientific	Cat# PA5-28922; RRID: AB_2546398
Rabbit-anti FBL	Cell Signaling Technology	Cat# 2639; RRID: AB_2278087
Rabbit-anti β-Actin	Cell Signaling Technology	Cat# 4970; RRID: AB_2223172
Goat Anti-Rabbit-HRP Conjugate	BioRad	Cat# 1705046; RRID: AB_11125757
Goat Anti-Mouse-HRP Conjugate	BioRad	Cat# 1705047; RRID: AB_11125753
Goat anti-Rabbit IgG (H+L) Cross-Adsorbed Secondary Antibody, Alexa Fluor™ 568	Invitrogen	Cat# A-11011; RRID: AB_143157
Goat anti-Rat IgG (H+L) Cross-Adsorbed Secondary Antibody, Alexa Fluor™ 647	Invitrogen	Cat# A-21247; RRID: AB_141778
Chemicals, peptides, and recombinant proteins		
EGF	Peprotech	Cat# AF-100-15
bFGF	Peprotech	Cat# 100-18B
Gem21	GeminiBio	Cat# 400-160
N2	GeminiBio	Cat# 400-163
Geltrex	Thermo Fisher Scientific	Cat# A1413202
BrdU	Sigma	Cat# B9285
Cycloheximide (CHX)	Sigma	Cat# C0934
Insulin	Sigma	Cat# I9278
SB431542	selleckchem	Cat# S1067
Y-27632	selleckchem	Cat# S1049
CHIR99021	selleckchem	Cat# S1049
A-83-01	selleckchem	Cat# S7692
LDN-193189	selleckchem	Cat# S2618
Critical commercial assays		
Click-&-Go® Plus OPP Protein Synthesis Assay Kits	Click Chemistry Tools	Cat# 1493
Pierce™ BCA protein assay kit	Thermo Fisher Scientific	Cat# 23225
SuperSignal West Pico PLUS Chemiluminescent Substrate	Thermo Fisher Scientific	Cat# 34579
RNA ScreenTape analysis	Agilent	Cat# 5067-5576
Ssofast EvaGreen supermix	BioRad	Cat# 1725200

(*Continued on next page*)

Continued

REAGENT or RESOURCE	SOURCE	IDENTIFIER
Recombinant DNA		
PB-CAG-EGFP-DKC1	N/A	This paper
PB-CAG-iFBL-GFP-Puro	N/A	This paper
PB-CAG-iFBL-C-GFP-Puro	N/A	This paper
PB-CAG-iChimeric FBL-GFP-Puro	N/A	This paper
PB-CAG-PMSB2-tdTomato	N/A	This paper
PB-CAG-RPL29-GFP	N/A	This paper
CAG-PBase	VectorBuilder	N/A
GFP-NPM WT	Xin Wang Lab	Addgene:17578; RRID:Addgene_17578
NLS-LucWT-GFP	Xiaolu Yang Lab	Addgene:127709; RRID:Addgene_127709
pEGFP-C1-Fibrillarin	Sui Huang Lab	Addgene:86766; RRID:Addgene_86766
pcsII-pb2-flag	Do-Hyung Kim Lab	Addgene:86766; RRID:Addgene_86766
PB-CAG-tdTomato	Mario Capecchi lab	Addgene:133569; RRID:Addgene_133569
PB_iNEUROD1_P2A_GFP_Puro	Prashant Mali Lab	Addgene:168803; RRID:Addgene_168803
pSpCas9(BB)-2A-Puro (PX459) V2.0	Feng Zhang Lab	Addgene:62988; RRID:Addgene_62988
Experimental models: Cell lines		
Human iPS cell line: CR0000010	NINDS Human Cell and Data Repository	N/A
Human iPS cell line: CR0000008	NINDS Human Cell and Data Repository	N/A
Human ES cell line: H9	Wisconsin International Stem Cell	N/A
Oligonucleotides		
SNORD118 gRNA-1 5′-ATCGTCAGAAAGAATCAGAT-3′	GENEWIZ	This paper
SNORD118 gRNA-2 5′-ATCGTCAGAAAGAATCAGAC-3′	GENEWIZ	This paper
ssODN: T*A*TCTGCTAATCAGCATAACACAAATG TAAGTGATCGTCACAAAGAATCAGATAG GAGCAATCAGGGTGTTGCAAGACCTGA TTACGCAGAGACGTT A*A*T(*Phosphorothioate modification)	GENEWIZ	This paper
Primers for qPCR	GENEWIZ	Table S1
DNA probes	GENEWIZ	Table S1
Software and algorithms		
Fiji	Image J	https://imagej.net/software/fiji/
GraphPad Prism 10	GraphPad	https://www.graphpad.com/
Leica Application Suite X	Leica	https://www.leica-microsystems.com/

RESOURCE AVAILABILITY

Lead contact

Any additional information and requests for resources and reagents should be directed to and will be fulfilled by the lead contact, Jian-Fu Chen (jianfu@usc.edu).

Materials availability

This study did not generate new unique reagents. All plasmids used in this study are available through the lead contact.

Data and code availability

- All data supporting the current study's findings are available in the article and its supplemental information. Data reported in this paper will be shared by the lead contact upon request.
- This paper does not report original code.
- Any additional information required to reanalyze the data reported in this work is available from the lead contact upon request.

EXPERIMENTAL MODEL AND STUDY PARTICIPANT DETAILS

Two human iPSC lines (CR0000010 and CR0000008) reprogrammed from healthy individuals were obtained from the NINDS Human Cell and Data Repository (NHCDR). H9 human ES cells were ordered from the Wisconsin International Stem Cell (WISC) bank. They have been characterized in our previously published studies.[33,34]

METHOD DETAILS

Human iPSC culture

The hPSCs were cultured in mTeSR-plus medium (Stem cell technologies, 100-0276) and seeded on a Geltrex (Thermo, A1413301)-coated culture dish. The hPSCs were detached from the dish by incubation with ReLeSR (Stem cell technologies, 05872) for 1 min at RT and 5 min in a 37°C incubator. The cells were then dissociated into small cell clusters by manual pipetting. The medium was changed every other day.

Genome editing

For genome targeting, gRNAs were designed using the online software CHOPCHOP (https://chopchop.cbu.uib.no/) and cloned into pSpCas9(BB)-2A-Puro (PX459) V2.0 vector. The gRNA (5'-ATCGTCAGAAAGAATCAGAT-3') or (5'-ATCGTCAGAAAGAATCAGAC-3') was used to generate the *SNORD118*$^{*5C>G}$ point mutation hiPSCs. Briefly, hiPSCs were treated with ROCK inhibitor Y27632 (10 μM, Selleckchem) for 24 h before electroporation. The cells were dissociated into single cells by using Accutase cell detachment solution (Millipore, SCR005). 10 μg plasmid (or with 1 μl 100 μM ssODN to introduce point mutation) were electroporated into 1.0×10^6 cells, using NEPA21 Electro-Kinetic Transfection Systems, then immediately seeded on Geltrex-coated plates and cultured in mTeSR-plus medium containing Y27632 (50 μM) for the first 24 h. Puromycin (0.5 μg/mL) was added to the medium for 2 days selection. Then hiPSCs were maintained in a medium without puromycin until colonies emerged. Individual colonies were picked up and expanded. PCR products were amplified and subjected to Sanger sequencing to identify mutant clones. The ssODN and primers used for hiPSCs genotyping are listed in Table S1.

Human neural progenitor cell (NPC) generation

Human NPCs were induced from hiPSCs as previously described with minor modifications. Briefly, hiPSCs were cultured until 80% confluence and then were passaged into cell aggregates to form embryoid bodies (EBs). These EBs underwent suspended culture for two weeks in a neural induction medium, which consisted of N2B27 medium supplemented with dual Smad inhibitors, SB431542 (10 μM) and LDN-193189 (0.1 μM) (Selleckchem). N2B27 medium was 50% DMEM/F12, 50% Neurobasal medium, 0.5% N2 supplement, 1% Gem21 supplement, 1% Glutamax, 0.2% Primocin, and 1% NEAA (Thermo Fisher Scientific). EBs were attached to the Geltrex-coated plates and cultured in a neural induction medium containing 20 ng/mL bFGF until the neural rosettes emerged. Neural rosettes were manually picked up and dissociated into individual cells by Accutase, which were then plated on Geltrex-coated plates. The NPCs were maintained in an N2B27 medium with 20 ng/mL bFGF and 20 ng/mL EGF, and the medium was changed every other day.

Generation of cerebral organoids

Cerebral organoid generation followed the published protocol with minor modifications. Briefly, hiPSC colonies were dissociated into single cells using Accutase. On day 1, a total of 9,000 cells were plated into each well of an ultra-low-attachment 96-well plate (Thermo) for single EB formation. The EB formation medium consisted of DMEM/F12, 20% Knockout Serum Replacement, 1% GlutaMAX, 1% NEAA, 50 μM Y27632, and 4 ng/mL bFGF (Perpotech). On day 4, the EBs were cultured in an EB formation medium without Y27632 and bFGF. On day 7, the EBs cultured in a neural induction medium for 5 days. The neural induction medium consisted of DMEM/F12, 0.5% N2 supplement, 1% GlutaMAX, 1% non-essential amino acids, 1% penicillin-streptomycin, and 10 μg/mL heparin with dual Smad inhibitors, A83-01(1 μM) and LDN-193189 (0.1 μM). On day 12, the EBs were embedded into Geltrex droplets and cultured for 4 days in a medium containing 50% DMEM/F12, 50% Neurobasal medium, 0.5% N2 supplement, 1% GEM21 supplement without Vitamin A, 1% GlutaMAX, 1% NEAA, 0.2% Primocin, and 2.5 ng/mL human insulin solution (Sigma). On day 16, the organoids were transferred to a spinner flask rotating continuously at 60 rpm and cultured in an N2B27 medium with 2.5 ng/mL human insulin. The medium was changed every week.

Generation of neural crest organoids

Human iPSCs were dissociated into single cells using Accutase, seeded at 9,000 cells/well in a low-attachment 96-well plate with mTeSR-plus medium containing 10 μM Y-27632, centrifuged at 1500 rpm for 5 min, and cultured with medium changes every other day to neural crest induction medium (N2B27 medium with 2 μM SB431542 and 1 μM CHIR99021). On day 12, the spheres were transferred to a low-attachment dish and maintained in N2B27 medium with 20 ng/mL EGF and 20 ng/mL bFGF on an orbital shaker in the CO_2 incubator at 37°C.

Real-time quantitative PCR

Total RNAs were extracted using an RNeasy Mini Kit (QIAGEN, 74104). The reverse transcription was performed using random primers and M-MLV Reverse Transcriptase (Promega, M1701). Quantitative RT-PCR analysis was performed using Ssofast EvaGreen supermix (Bio-Rad) and detected with Bio-Rad CFX96 Optics Module qPCR/RT PCR Thermal Cycler. The data were analyzed using the comparative CT ($2^{-\Delta\Delta CT}$) method. The ΔCT was calculated using β-actin as the internal control. All experiments were performed with three biological replicates. Primer sequences were provided in Table S1.

Immunostaining

For human NPC immunostaining, cells were fixed in 4% PFA for 15 min at RT, washed twice with Dulbecco's Phosphate-Buffered Saline (DPBS), and then incubated with primary antibodies in blocking buffer (2% goat serum + 1% BSA + 0.1% TritonX-100 in DPBS) overnight at 4°C before secondary antibody incubation. Cerebral organoids were fixed in 4% PFA for 30 min at room temperature. Cerebral organoids were washed three times with DPBS, incubated in 30% Sucrose solution at 4°C overnight, and then embedded in O.C.T. solution, followed by dry ice freezing. The frozen cerebral organoids were sectioned into 10 μm thick slices for immunostaining. The primary antibodies are listed in the key resources table. The secondary antibodies used were Alexa 488, Alexa 568, and Alexa 647 conjugated to specific IgG types (Invitrogen Molecular Probes).

BrdU labeling and EdU assay

Cerebral organoids were incubated in the medium containing BrdU (100 μM) for 2 h in the CO_2 incubator at 37°C. Then the cerebral organoids were washed by DPBS and fixed in 4% PFA for 30 min at RT. The samples were stained with BrdU antibody after sectioning. The BrdU-positive cells were counted by Image J software. EdU assay was performed by using the Click-&-Go EdU Cell Proliferation Assay Kit. Briefly, the cells were treated with EdU (10 μM) for 1 h, fixed with 4% PFA at RT for 15 min, and then incubated with 0.5% TritonX-100 in DPBS for 20 min. The EdU was detected by the reaction cocktail following the manual.

O- propargyl-puromycin (OPP) incorporation assay

OPP assay was performed by using Click-&-Go® Plus OPP Protein Synthesis Assay Kits. Briefly, the cells were treated with OPP (20 μM) for 20 min, fixed with 4% PFA at RT for 15 min, and then incubated with 0.5% TritonX-100 in DPBS for 20 min. The OPP was detected by the reaction cocktail following the manual. Finally, the cells were stained with Hoechst33342. The OPP intensity of cells was measured by Image J software.

Polysome profiling

The NPCs (5×10^7 cells) were treated with 0.1 mg/mL cycloheximide (CHX) for 10 min at 37°C, dissociated with Accutase for 5 min, and washed twice with 0.1 mg/mL CHX in 1 X DPBS. The cells were then lysed using a buffer containing 25 mM Tris-HCl pH 7.4, 5 mM MgCl2, 100 mM NaCl, 0.1 mg/mL CHX, 1% Triton X-100, 40 U/μL RNase inhibitor, 1 mM DTT, and 1× protease inhibitor. The lysate was incubated on ice for 10 min, followed by centrifugation at 13,000 × g for 10 min at 4°C. Sucrose gradients were prepared using 5% and 50% sucrose solutions, diluted in a sucrose buffer consisting of 25 mM Tris-HCl pH 7.4, 5 mM MgCl2, 100 mM NaCl, 0.1 mg/mL CHX, 40 U/μL RNase inhibitor, and 1 mM PMSF, all prepared in DEPC-treated water. The clear supernatants from the lysed cells were loaded onto the top of 10 to 50% sucrose gradients and centrifuged at 220,000×g (SW40 rotor, Beckman) for 3 h at 4°C. Sucrose gradient fractions were manually collected into a 96-well plate, and the absorbance was monitored at 260 nm using the SpectraMax i3x Multi-Mode Microplate Reader to analyze the polysome profile.

RNA ScreenTape analysis

Total RNA was isolated using Trizol and the concentration was measured with a Nanodrop (Thermo). Samples were diluted to 100 ng/mL using RNase-free water, and then 1 μl was loaded onto RNA ScreenTape for analysis by the Agilent TapeStation system. Samples with an RNA Integrity Number (RIN^e) greater than 9 were selected for mature 28S/18S ratio analysis using the TapeStation system Software A.01.05 (SR1).

RNA-protein interaction assay

The NPCs (1×10^8 cells) were irradiated with UV at 200 mJ and subsequently chilled with cold DPBS. Cell pellets were collected by centrifugation, weighed, flash frozen in liquid nitrogen, and stored at -80°C until analysis. For lysis, the pellets were thawed and resuspended in lysis buffer (50 mM Tris-HCl pH 7.0, 10 mM EDTA, 1% SDS, 40 U/μL RNase inhibitor, and 1× protease inhibitor cocktail). The resulting clear supernatants were pre-cleared using 30 μL of C-1 magnetic beads. The 1 mL of pre-cleared supernatant was then transferred to a 15 mL Falcon tube and 2 mL of hybridization buffer containing either anti-sense DNA probes or non-interacting negative probes labeled with BiotinTEG (100 pmol probe per 1 mL sample) was added. This mixture was incubated at 37°C overnight with shaking. Subsequently, 100 μL of C1-magnetic beads, pre-washed three times with lysis buffer, were added to the hybridization reaction and incubated at 37°C for 30 min with shaking. The beads were then isolated using a DynaMag magnetic strip and washed three times with washing buffer (10 mM Tris-HCl pH 7.0, 300 mM LiCl, 0.5% Nonidet-P40, 1× protease inhibitor cocktail), each wash lasting 5 min at 37°C with shaking. Finally, the beads were boiled in western blot loading buffer, and the supernatants were collected for western blot analysis. Details of the probes used are listed in Table S1.

QUANTIFICATION AND STATISTICAL ANALYSIS

Image analysis and quantification

The percentage of marker-positive cells was calculated by dividing the number of positive cells by the total cell count. The mean intensity per cell of a marker was determined by dividing the integrated density (InDent) by the number of cells. This value was used to calculate the fold change of a marker intensity, with the mutant group normalized against the control group. The images were all analyzed by the Image J software.

Statistical analysis

Statistical analysis was performed using GraphPad Prism. Significance was determined by two-tailed t-tests or one-way ANOVA, as indicated in the figure legends. Values are presented as mean $\pm$ SEM, with $p < 0.05$ considered significant. Significance levels are marked as $*p < 0.05$, $**p < 0.01$, $***p < 0.001$, and $****p < 0.0001$.